IOP Publishing

Journal of Physics D: Applied Physics

J. Phys. D: Appl. Phys. **51** (2018) 325002 (16pp)

https://doi.org/10.1088/1361-6463/aacfcf

Measurements of Gilbert damping parameter α for CoPt-based and CoFe-based films for magnetic recording applications

U.S.D.C. CENTRAL DISTRICT OF CALIFORNIA

CASE NO. 8:22-cv-01599-JVS-DFM

MR Technologies, GMBH

VS. Western Digital Technologies, Inc.

JOINT EXHIBIT JX-2036

DATE IDEN.

DATE EVID.

BY

Deputy Clerk

C Papusoi[1,3], T Le[1], C C H Lo[1], C Kaiser[2], M Desai[1] and R Acharya[1]

[1] Western Digital, 1710 Automation Parkway, San Jose, CA 95131, United States of America

[2] Western Digital, 44100 Osgood Road, Fremont, CA 94539, United States of America

E-mail: cristian.papusoi@wdc.com

Received 16 May 2018, revised 20 June 2018

Accepted for publication 28 June 2018

Published 13 July 2018

Abstract

Time-resolved MOKE (TRMOKE) and Q-band ferromagnetic resonance (FMR) are used to evaluate the damping parameter α and the magnetic anisotropy field $H_K = 2K/M_S$ (where K is the uniaxial anisotropy constant and M_S is the saturation magnetization) of CoPtX–Y and CoPtX (where X is non-magnetic element and Y denotes oxide(s)) granular alloys with perpendicular magnetic anisotropy and variable Co/Pt atomic ratio R. It is found that α monotonically increases in the range of 0.03–0.07 with decreasing R in the range of 2.5–5.5. By comparing the CoPtX films sputter-deposited in Ar and in Ar+O_2 atmosphere, it is found that α is less sensitive than H_K to the presence of non-magnetic additives (Cr, B) in the grain core. This suggests that α is much less sensitive than K to perturbations of d-electron band structure. FMR and TRMOKE are also used to evaluate α of magnetically soft CoFeX alloys. It is shown that adding 2 at.% Tb to CoFeX leads to an increase of α from 0.012 (undoped case) to 0.048, and a negative shift of the resonance field which is linearly dependent on the RF frequency. This effect, similar to that previously reported on Tb-doped NiFe films, is attributed to the highly anisotropic Tb 4f–5d exchange coupling. A synthetic-antiferromagnetic trilayer CoFeX (7 nm)/Ru (0.8 nm)/CoFeX (7 nm) is investigated by FMR. The interlayer RKKY coupling constant, evaluated from the frequency shift between the acoustic (symmetric) and optic (antisymmetric) resonance modes is $J_{EX} = 0.11$ erg cm^{-2}. The α value corresponding to the acoustic mode (0.016) matches that of a single-layer CoFeX film whereas the optic mode shows a higher α (0.0265). This is interpreted to be a consequence of spin-pumping through the Ru interlayer. The evaluated spin mixing conductance for the CoFeX/Ru interface is $\tilde{g}^{FN}_{\uparrow\downarrow} = 22.5\,\mathrm{nm}^{-2}$.

Keywords: time-resolved MOKE (TRMOKE), ferromagnetic resonance (FMR), microwave assisted magnetic recording (MAMR)

Introduction

In perpendicular magnetic recording (PMR), achieving high recording densities is enabled by decreasing media grain volume V and increasing the media magnetic anisotropy constant K in order to provide a reasonably high thermal stability at ambient temperature T_{RT} so that $KV/(k_B T_{RT}) > 65$. Since recording occurs on a short time scale (~1 ns), the medium coercivity and saturation field approach the anisotropy field $H_K = 2K/M_S$ where M_S is the saturation magnetization. The magnetic recording layers of PMR media typically have H_K ~ 20 kOe. Such high values of H_K impose a constraint on the minimum switching field H_{SW} that the recording head should provide in order to switch the grain magnetization from one orientation to the other along the easy-axis. Various methods to decrease H_{SW} have been explored, including the exchange

[3] Author to whom any correspondence should be addressed.

© 2018 IOP Publishing Ltd Printed in the UK

HIGHLY CONFIDENTIAL - ATTORNEYS' EYES ONLY

MR Technologies GmbH
Ex. 2018, IPR2026-00016
Page 1 of 16

WD0293673

JX-2036.001

coupled composite (ECC) media structure [1–3] and energy-assisted recording schemes involving the application of RF fields [4–6] or heat [7, 8]. In addition to the strength of H_{SW}, switching properties of a ferromagnetic film also depend on the Gilbert damping constant α of the medium defined in the LLG equation. The damping constant α has a direct impact on the time required for the magnetization to stabilize along a direction of minimum energy subsequent to a perturbation of its orientation. The number of magnetization precessions prior to switching is enhanced for media with a low α.

Current PMR media have an ECC structure consisting of several magnetic layers having a vertically graded anisotropy which enables the reduction of H_{SW} via an exchange spring effect [1]. One way to tailor the value of H_K of each layer in a PMR stack is to adjust the Co/Pt atomic ratio, typically in the range 2–6. Since the ECC structure is expected to remain one of the key features of future PMR media, it is important to investigate the effects of Co/Pt atomic ratio on H_K and α of CoPt-based films, which is the main goal of the present work. While the dependence of H_K on Co/Pt ratio has been extensively studied [9, 10], the effect of Co/Pt ratio on α has been scarcely investigated in the past. Q-band FMR measurements on epitaxial CoCrPt films with in-plane anisotropy [11] reported $\alpha = 0.038$ for $Co_{81}Cr_{15}Pt_4$ and $\alpha = 0.042$ for $Co_{73}Cr_{19}Pt_8$ alloys. Time-resolved MOKE (TRMOKE) measurements on $Co_{65}Cr_{15}Pt_{20}$ films with perpendicular anisotropy reported $\alpha = 0.054$ [12]. The increase of α with increasing Pt content is attributed to the strong spin–orbit coupling of Pt atoms causing spin-flip and spin-dependent scattering of conduction electrons [13].

In PMR, a magnetically soft-underlayer (SUL), located below the magnetic recording layer(s), is used to enhance the field acting on the recording layer(s) by bringing them into the gap of the recording head [14]. Current PMR media often employ synthetic antiferromagnetic SULs (SUL–SAF) with the structure SUL/Ru/SUL, which consist of two SUL layers antiferromagnetically coupled through a Ru layer that intermediates an RKKY antiferromagnetic coupling. SUL–SAF were shown to have the advantage over a single-layer SUL of reducing the readback noise as a consequence of minimizing the magnetostatic coupling between the recording layers and the SUL, as well as a reduction of the in-plane size of the magnetically perturbed region in the SUL during and after the writing process [15]. LLG simulations indicate that damping in the SUL has an effect on the SUL magnetization settling time subsequent to field application by the recording head. The lower is α in the SUL, the larger is the magnetically perturbed region in the SUL during the writing process, which could reverse grains in the recording layer via the magnetostatic coupling between the two, leading to readback noise in the recorded patterns (jitter or transition noise) [16]. This noise could potentially become more important with increasing recording density. Therefore, α in the SUL needs to be enhanced, ideally without any loss of its soft magnetic properties.

In this work, TRMOKE and ferromagnetic resonance (FMR) are used to evaluate α and H_K of CoPt-based granular films with various Co/Pt atomic ratios, and of magnetically soft CoFe-based SUL films. Both measurement techniques are found to offer consistent values of α of the films. For the CoPt-based granular films, it is found that α increases monotonically from 0.03 to 0.07 as the Co/Pt ratio decreases from 5.5 to 2.5. For the single-layer CoFe-based SUL films (SUL–SL), α is found to increase by a factor of four (from 0.012 to 0.048) without significantly changing the hysteresis loop shape as a result of doping the CoFe-based films with 2 at.% Tb. This observation, important for PMR media development, is in agreement with the previous results on Tb-doped NiFe [17] that associates the increase of α with the strong contribution of the anisotropic exchange interaction between 4*f*–5*d* electrons to the magnetic anisotropy of Tb. The present results indicate the potential use of Tb doping to enhance damping of SUL without degradation of its soft magnetic properties. In the case of SUL–SAF, both the acoustic and optic resonance modes are detected in the FMR spectra. The optic mode features a higher α than that of the acoustic mode, which is attributed to spin-pumping through the Ru spacer. The spin mixing conductance of the SUL/Ru interface is estimated from α and is found to be close to the value for Py/Ru interface.

Experimental details

Sample preparation

Samples investigated in the study, described in table 1 and schematically depicted in figure 1, are deposited in Ar atmosphere using an industrial sputtering system with a base pressure better than 1×10^{-7} mTorr. Samples are deposited at 120 °C on NiP-plated Al disk substrates 65 mm in diameter for TRMOKE measurements and on 65 mm-diameter glass substrates for FMR measurements. Two types of alloys are investigated: (i) CoPt-based alloys with strong perpendicular magnetic anisotropy that are used as recording layers in PMR media, and (ii) an amorphous CoFe-based alloy with low in-plane anisotropy that is used as SUL. The CoPt alloys are of two types:

(a) CoPtX–Y alloys (samples denominated in the following by MAG and MAG1–5), where X is a non-magnetic metal such as Cr, and Y is an oxide, e.g. SiO_2, TiO_2, etc, or a mixture of oxides that segregates along the boundaries of the CoPtX grains and in turn helps reduce the exchange coupling among the magnetic grains. Several compositions with Co/Pt atomic ratios in the range of 3–5.5 are investigated in this work.
(b) CoPtX alloys (samples denominated by CAP1, CAP2, CAP2R), where X is a non-magnetic metal such as Cr and the Co/Pt atomic ratio falls in the range of 2.3–2.4.

The CoPtX alloys, which are often used to form the uppermost magnetic layer(s) in PMR media to promote magnetization switching, feature a stronger intergranular exchange coupling than the CoPtX–Y alloys with oxide segregants. This is motivated by the following two requirements for the top recording layer in PMR media: (a) it

HIGHLY CONFIDENTIAL - ATTORNEYS' EYES ONLY
MR Technologies GmbH
Ex. 2018, IPR2026-00016
Page 2 of 16
WD0293674
JX-2036.002

Table 1. Sample description and the values of M_S, H_K, and α determined from the TRMOKE, FMR and VSM measurements.

Experiment	Sample	Co/Pt ratio (at.)	M_S (emu cm^{-3})	H_K (Oe)	α
TRMOKE	MAG1	3	815	19953 ± 95	0.0512 ± 0.0018
	MAG2	3.45	833	19448 ± 98	0.046 ± 0.0017
	MAG3	4	914	17778 ± 123	0.035 ± 0.0006
	MAG4	3.9	871	16041 ± 85	0.0365 ± 0.0018
	MAG5	5.36	641	14892 ± 47	0.0358 ± 0.0019
	CAP1	2.33	498	11395 ± 210	0.07 ± 0.0029
	CAP2	2.4	582	14103 ± 122	0.0647 ± 0.0016
	CAP2R	2.4	703	17636 ± 83	0.066 ± 0.0014
	SUL–SL	—	496 ± 7 496 (VSM)	—	0.0144 ± 0.0005
FMR	MAG	3.24	800	20647 ± 88	0.0435 ± 0.0053
	SUL–SL	—	495 ± 3.3	11.9 ± 2	0.012 ± 0.0005
	SUL+Tb–SL	—	505 (VMS)	—	0.048 ± 0.0011
	SUL–SAF	—	496	—	0.016 ± 0.0001 (a) 0.0265 ± 0.0004 (o)

should have the lowest H_{SW} among the layers of the PMR stack in order to initiate the magnetization switching, and (b) it should reduce the grain switching field distribution (SFD) of the PMR stack by introducing a stronger and more homogeneous lateral exchange coupling between magnetic grains than that in the other recording layers with grain boundary segregation.

The structure of CoPtX–Y and CoPtX samples used in this study is: substrate/seed/Ru (20 nm)/CoPtX–Y or CoPtX (10 nm)/C (figure 1(a)). One of the CoPtX alloys with a Co/Pt ratio of 2.4 is either deposited in pure Ar (sample CAP2, table 1) or reactively sputtered in Ar+2% O_2 (sample CAP2R). The purpose is to check the effects on H_K and α of the CoPtX alloy of segregating the non-magnetic species X (e.g. Cr) from the grain core by means of preferential oxidation of X.

The groups of SUL samples based on an amorphous CoFeX alloy where X are refractory metals with large atoms such as Ta, Zr, etc, are prepared to have the following structures:

(a) Single-layer SUL: substrate/CoFeX (10 nm)/C (figure 1(b)), denominated in the following by SUL–SL. The effect of Tb doping on α of the SUL alloy is investigated by sputter-deposition of a single-layer SUL sample, denominated in the following by SUL+Tb–SL, using a CoFeX target doped with 2 at.% Tb.
(b) Synthetic antiferromagnetic SUL: substrate/CoFeX (7 nm)/Ru/CoFeX (7 nm)/C (figure 1(c)) denominated in the following by SUL–SAF.

The effective perpendicular anisotropy field $H_K^{eff} = H_K - 4\pi M_S$ and the damping parameter α are evaluated using TRMOKE for MAG1–5, CAP1, CAP2, CAP2R, SUL–SL, and FMR for MAG, SUL–SL, SUL+Tb–SL and SUL–SAF (table 1). The interlayer RKKY exchange coupling J_{EX} for SUL–SAF is evaluated using FMR. Hysteresis loops and saturation magnetization M_S are measured using a 2 T vibrating sample magnetometer (VSM). The details of the FMR and TRMOKE measurements are given in the following sections.

FMR measurements

FMR experiments are performed in the radio-frequency (RF) range of 5–40 GHz (Q-band) using a broadband microwave generator and a coaxial microwave track with the sample mounted on a coplanar waveguide (CPW) [18]. The DC (bias) field is applied using an electromagnet. The sample is placed face-down on the CPW located between the pole pieces of the electromagnet. The RF transmission output of the CPW is converted into a DC voltage using a planar-doped barrier diode detector. Measurements are performed at fixed RF frequency by stepping the DC field through resonance. An AC modulation field is applied along the DC field and the output signal is detected using a lock-in method to enhance the measurement sensitivity. The frequency of the AC modulation field is 100 Hz and the modulation amplitude is 10–50 Oe. The step in the DC field is selected to be larger than the amplitude of the AC modulation field. As explained in appendix B, the measured signal is proportional to $d\chi_{RF}/dH$ where H is the intensity of the DC field and χ_{RF} is the imaginary component of the RF susceptibility.

TRMOKE measurements

The schematics of the in-house built TRMOKE setup used in this study is presented in figure 2. In TRMOKE experiments [19], a mode-locked Ti-sapphire laser ($\lambda = 800$ nm) is used to generate repetitive pulses having 100 fs duration and 12.5 ns period. The laser beam is split into two beams, namely the pump and probe beams, by using a half-wavelength plate and a polarizing beam-splitter (BS). The orthogonal orientation of the two beam polarizations is prerequisite for obtaining a high signal/noise ratio (SNR) of the TRMOKE signal. The probe beam passes through a second harmonic generator (SHG) that reduces its wavelength to 400 nm, and further through an optical delay line (ODL) that varies the length of its optical path by a controlled amount using a stepping motor to adjust the position of a retro-reflecting mirror

HIGHLY CONFIDENTIAL - ATTORNEYS' EYES ONLY
MR Technologies GmbH
Ex. 2018, IPR2026-00016
Page 3 of 16
WD0293675
JX-2036.003

sliding on an optical rail. The position of the retro-reflecting mirror thereby controls the time delay between the pump and probe pulses. The pump beam passes through an electro-optical modulator (EOM) that RF modulates its intensity at an RF frequency $\Omega = 1$–10 MHz. The RF modulation is used to improve the SNR of the measurements by reducing the contribution of the $1/f$ noise of the mode-locked laser. The pump and probe beams are combined using a dichroic mirror (DM) and focused on the sample within a spot diameter of ~2.5 μm FWHM. The fluences of the two laser beams at the sample surface are 0.7 mJ cm^{-2} for the pump beam and 0.15 mJ cm^{-2} for the probe beam. After reflecting from the sample, the probe beam passes through a half-wave plate (HWP) and then through a Wollaston prism (WP) that splits it into two perpendicularly polarized beams which are incident on a dual photodetector (DD). The differential output signal of the photodetector is proportional to the component of the sample having magnetization perpendicular to the sample plane via the polar Kerr effect (i.e. the TRMOKE signal). The latter is measured as a function of the delay between the pump and probe pulses, using a phase sensitive lock-in amplifier (LIA). However, the signal detection utilizing an RF LIA is noisy due to its large detection bandwidth. As explained in [20], audio-frequency (AF) LIAs feature a lower noise than RF LIAs. In order to take advantage of this feature of AF LIAs, a double modulation detection scheme is employed. In addition to the pump beam being modulated at the RF frequency Ω, the probe beam is also modulated at an AF frequency $\omega = 500$ Hz using an optical chopper (CH). In this case, the output signal of the dual photodetector has two side-bands at $\Omega - \omega$ and $\Omega + \omega$. A double-balanced mixer (DBM) is connected between the output of the dual photodetector and the input of the AF LIA. The local oscillator input of the DBM is connected to the TTL output of the RF oscillator used to modulate the pump beam at the RF frequency Ω, and the signal input of the DBM is connected to the output of the dual photodetector. As a result, the output signal of the DBM is modulated at ω and $2\Omega \pm \omega$. The low frequency ω component of the DBM output signal is measured with a high SNR by an AF LIA using the TTL output of the probe beam modulator (optical chopper) as a reference.

The region of the sample exposed to the pump/probe beams is also subjected to an applied DC magnetic field H having adjustable intensity and orientation with respect to the sample plane. The field is generated by a permanent magnet capable of delivering a maximum field of 7 kOe at a distance of 1 mm away from the face of the magnet pole piece. The DC field is applied from the side of the sample (65 mm diameter disk) opposite to that exposed to the laser beams. The magnet is mounted on a goniometer having the center of rotation coinciding with the center of the laser beam spot on the sample surface. This geometry allows an independent control of the field orientation by adjusting the goniometer angle, and of the field intensity by translating the magnet along the radius of the goniometer using a linear stage.

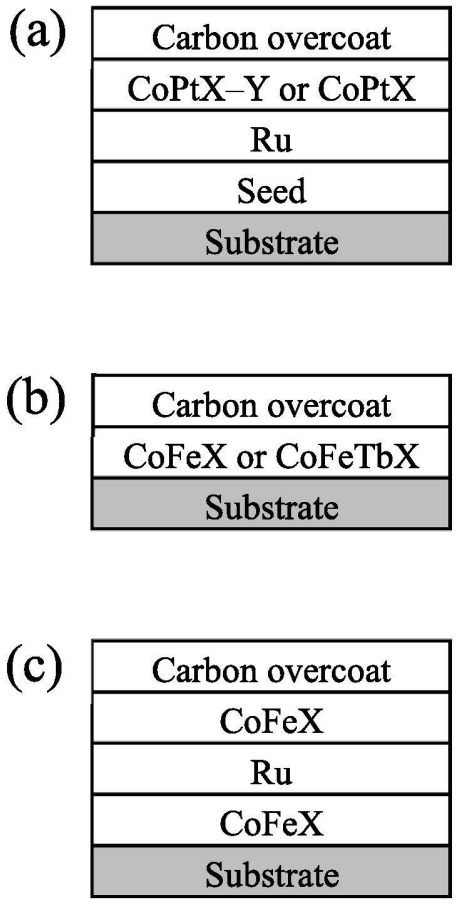

Figure 1. Sample structure: (a) MAG, MAG1–5 (CoPtX–Y) and CAP1,2,2R (CoPtX); (b) SUL–SL (CoFeX) and SUL+Tb–SL (CoFeTbX); (c) SUL–SAF (CoFeX/Ru/CoFeX).

Results

As shown in figure 3(a), the CoPtX-Y samples require a substantial saturation field, usually above 7 kOe (i.e. larger than the maximum field available in the TRMOKE setup). Therefore, samples MAG1-5 are first saturated perpendicular to the film plane using a 2 T electromagnet prior to performing TRMOKE measurements. For samples with perpendicular anisotropy, the selection of the optimal applied field orientation must take into account the following two factors:

(1) As the angle of the applied field relative to the perpendicular to the film plane increases, the oscillation amplitude of the magnetization component perpendicular to the film plane increases. Therefore, the magnetization oscillation can be detected with a higher SNR by polar Kerr effect.
(2) If the field angle is too large, the film can be partially demagnetized. This is due to the combined effect of the high M_S and the presence of grain segregation in the CoPtX-Y samples that leads to the dominance of magnetostatic over the exchange interactions between grains. Partial demagnetization may result in an inaccurate estimation of α based on the assumption of the fundamental mode.

HIGHLY CONFIDENTIAL - ATTORNEYS' EYES ONLY
MR Technologies GmbH
Ex. 2018, IPR2026-00016
Page 4 of 16
WD0293676
JX-2036.004

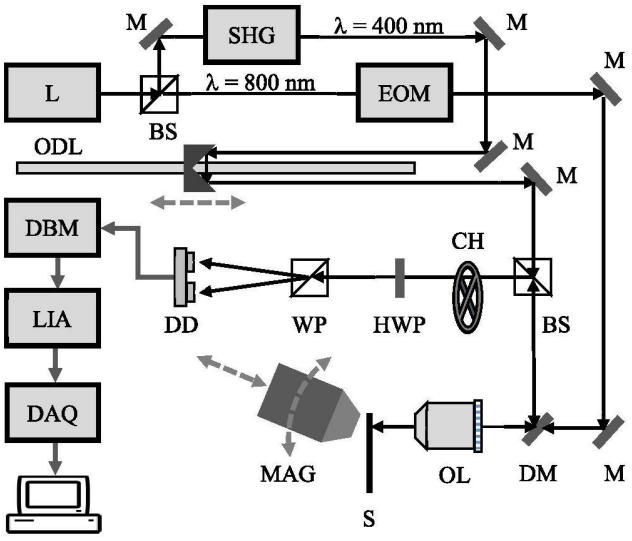

Figure 2. Schematics of the TRMOKE setup, containing: Ti-sapphire pulsed laser (L), second harmonic generator (SHG), electro-optical modulator (EOM), optical delay line (ODL), dichroic mirror (DM), mechanical chopper (CH), half-wave plate (HWP), Wollaston prism (WP), dual detector (DD), objective lens (OL), beam splitters (BS), mirrors (M), magnet (MAG), sample (S), double-balanced mixer (DBM), lock-in amplifier (LIA) and data acquisition card (DAQ).

In order to determine the largest applied field angle that can be used while still preserving the saturated magnetization state, the following VSM experiment is carried out on the CoPtX-Y and CoPtX samples. First a DC field of 20 kOe is applied along the easy-axis (i.e. perpendicular to the film plane) in order to saturate the film magnetization, and then removed. The remanent magnetization M_{RS} is measured. Then a DC field of 7 kOe (equals to the maximum field achievable in TRMOKE) is applied at an angle ψ with respect to the perpendicular to film plane, and then removed. Remanent magnetization M_R perpendicular to the film plane is then measured. The experiment is repeated for several values of ψ in the range of 0–90°. The dependence of the normalized remanent magnetization M_R/M_{RS} on ψ is presented in figure 3(b) for MAG1, MAG3, MAG5, CAP2 and CAP2R. According to figure 3(b), in non-segregated films having low M_S values, such as CAP1 and CAP2, the tilt of the applied field ψ can be as large as 70° before the samples become partially demagnetized as indicated by the observed decrease in M_R/M_{RS}. In contrast, for the CoPtX-Y samples (MAG, MAG1-5) having high M_S and a high segregant content, M_R/M_{RS} starts to decrease for applied field angle ψ greater than ~40°. According to these observations, the applied field angle ψ is fixed at 40° for samples MAG1–5 and 60° for CAP1, CAP2 and CAP2R. For the SUL samples, the selection of applied field angle is less critical and ψ is set to 20° to enhance the TRMOKE signal.

TRMOKE

In TRMOKE experiments, the energy of a 100 fs pump pulse ($\sim 10^{-10}$ J) is transferred to the ferromagnetic sample within a narrow spot diameter, causing a local heating effect [21].

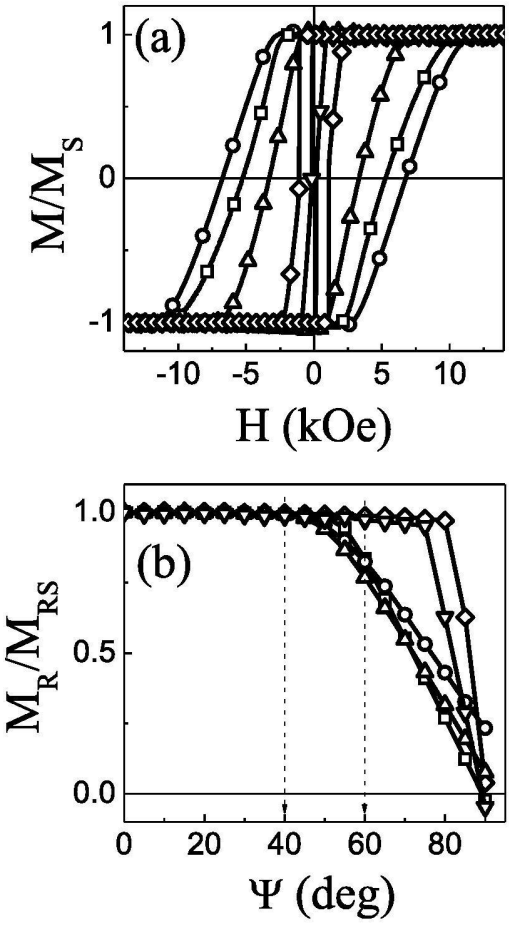

Figure 3. (a) Easy-axis hysteresis loops for samples MAG1 (○), MAG3 (□), MAG5 (△), CAP2 (▽) and CAP2R (◇) measured using polar-Kerr effect. (b) Remanent magnetization M_R (normalized to M_{RS}, where M_{RS} is the saturation remanent magnetization) measured along the direction perpendicular to the film plane subsequent to the application of $H = 7$ kOe under an angle Ψ with respect to the perpendicular to the film plane for samples MAG1 (○), MAG3 (□), MAG5 (△), CAP2 (▽) and CAP2R (◇).

M_S and H_K of the heated region undergo an ultrafast decrease, leading to a sudden change in the orientation of the effective magnetic field H_{eff} that includes the anisotropy, magnetostatic, exchange and applied field contributions. As a result, M_S becomes non-collinear with H_{eff}. Thermal equilibrium of the electrons, phonons and spins is reestablished in a few ps after the application of the pump pulse. Once thermal equilibrium is reestablished, the easy axis of the ferromagnetic sample returns to the original orientation it had before excitation and M_S starts to precess around a constant H_{eff} before aligning with H_{eff}. Magnetization precession is evidenced by the polar-Kerr effect using a low energy probe pulse which is delayed by t (that can be adjusted with ~1 ps resolution) with respect to the application of the pump pulse. The recovery of M_S is delayed by the heat diffusion in the sample and it usually completes in ~20 ps after the application of the pump pulse [22], as suggested by the invariance of the M_S oscillation period for time delays $t > 20$ ps. Therefore, in the fit of TRMOKE data the evolution of M_S during the first 20 ps after the application of

HIGHLY CONFIDENTIAL - ATTORNEYS' EYES ONLY
MR Technologies GmbH
Ex. 2018, IPR2026-00016 WD0293677
Page 5 of 16
JX-2036.005

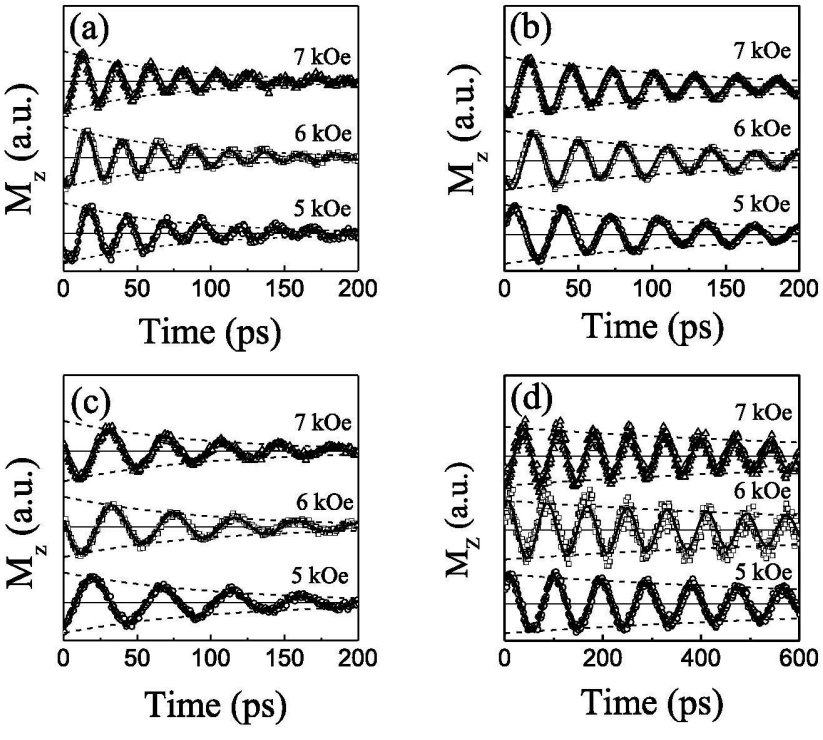

Figure 4. TRMOKE measurement of the component of film magnetization perpendicular to the film plane as a function of the delay between the pump and probe laser pulses for samples (a) MAG1, (b) MAG5, (c) CAP1, and (d) SUL–SL. For each sample, three magnetization time traces are presented (symbols) that correspond to $H = 5$ kOe (○), 6 kOe (□) and 7 kOe (△); their fit using a damped periodic function (equation (1)) (solid line) and the envelope of the magnetization oscillations used to extract the damping time τ (dashed lines) are also presented.

the pump pulse is disregarded and the time origin for the pump-probe delay t is shifted by the same amount. Magnetization relaxation subsequent to the anisotropy field pulse takes place not only through coherent oscillations but also through incoherent phonon and magnon relaxation processes [23]. The latter leads to a background signal displaying an exponential time decay. For a fixed value of the applied field H and orientation ψ with respect to the perpendicular to film plane (Oz), the pump-probe delay t is varied in the range of 0–500 ps. The magnetization component perpendicular to the film plane M_Z, probed by polar-Kerr effect, is recorded as a function of t and fitted using a damped harmonic oscillatory function having the expression [19]:

$$M_Z(t) = A\sin(2\pi ft + \phi)\, e^{-\frac{t}{\tau}} + Be^{-\frac{t}{\tau_B}} + C \qquad (1)$$

where A, f, ϕ, τ are the precession amplitude, oscillation frequency, initial phase and oscillation damping time, respectively, and B, τ_B, C are the background amplitude, damping time of the background signal and offset, respectively. The parameters A, B, C, f, ϕ, τ, τ_B are extracted via a least-squares fit of $M_Z(t)$ using equation (1). After subtracting the background, the pure oscillatory component of the TRMOKE signal $M_Z = A\sin(2\pi ft + \phi)\exp(-t/\tau)$ is presented in figures 4(a)–(d) for samples MAG1, MAG5, CAP1, SUL–SL and several values of the applied field H. The extracted field dependencies $f(H)$ and $\tau(H)$ are fitted using equations (A.8*a*) and (A.8*b*) derived in the appendix A in order to extract H_K^{eff} and the damping parameter α. During the fit, the values of the Landé factor are fixed at $g_L = 2.153$ for MAG1–5, CAP1, CAP2, CAP2R and $g_L = 2.13$ for SUL–SL as determined by FMR for MAG and SUL–SL. The experimental and theoretical $f(H)$ for samples MAG1–5 are presented in figure 5(a), for samples CAP1, CAP2, CAP2R in figure 5(c) and for SUL–SL in figure 5(e). The corresponding $\tau(H)$ dependencies are presented in figures 5(b), (d) and (f). The saturation magnetization M_S for samples MAG1–5 and CAP1, CAP2, CAP2R is measured by magnetometry (VSM) and the anisotropy field H_K is evaluated as $H_K = H_K^{eff} + 4\pi M_S$. The determined values of M_S, H_K and α are presented in table 1.

The values of H_K and α are plotted in figure 6 as a function of the Co/Pt ratio for the CoPtX–Y and CoPtX samples. Figure 6 shows that damping monotonically increases with decreasing Co/Pt ratio. This can be interpreted based on the following mechanism. The Co 3*d* electrons hop onto Pt sites and spin polarize the Pt 5*d* electrons [24]. As a result, Pt atoms acquire a magnetic moment and contribute to damping via the strong spin–orbit coupling of the Pt 5*d* electrons according to the breathing Fermi surface model of Kambersky [25]. As one can notice in figure 6 and table 1, in the case of CoPtX alloy both H_K and M_S are higher for the reactively sputtered sample CAP2R than for the non-reactively sputtered CAP2. As a result of O_2 addition to the sputter gas, non-magnetic species like Cr and B originally present in the grain core are oxidized and segregated along the grain boundaries. This leads to a perturbation of the 3*d* electronic band structure of the grain core, which results in an increase of H_K and M_S. According to

HIGHLY CONFIDENTIAL - ATTORNEYS' EYES ONLY
MR Technologies GmbH
Ex. 2018, IPR2026-00016
Page 6 of 16
WD0293678
JX-2036.006

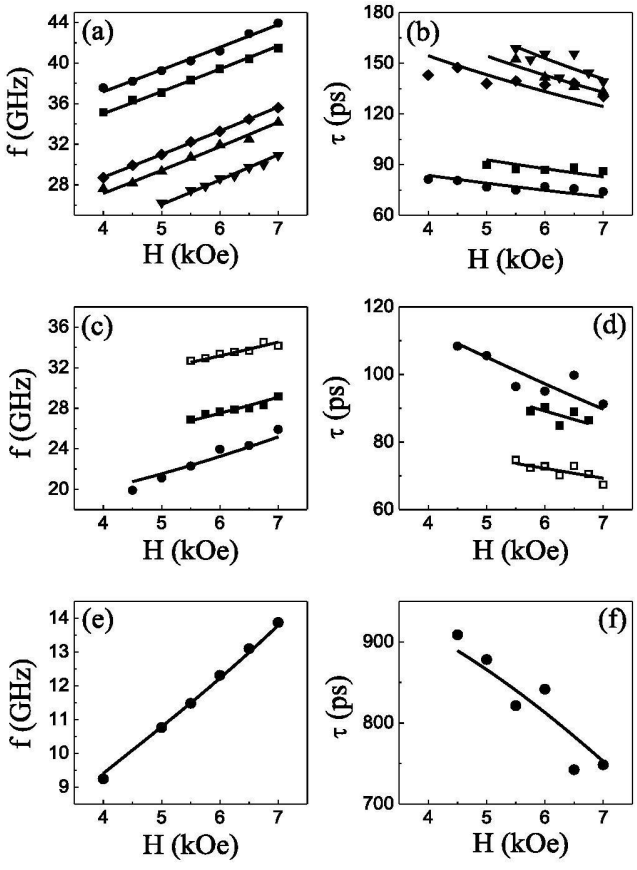

Figure 5. Magnetization oscillation frequency f ((a), (c) and (e)) and damping time τ ((b), (d) and (f)) as a function of the applied field H for samples MAG1 (●), MAG2 (■), MAG3 (▲), MAG4 (▼) and MAG5 (♦) (shown in (a) and (b)); CAP1 (●), CAP2 (■) and CAP2R (□) (in (c) and (d)), and SUL–SL (●) (in (e) and (f)) evaluated by TRMOKE.

figure 6, the damping parameter α appears to be less affected by the oxidation process, suggesting that α is less sensitive to the modification of the electronic band structure of grain core by non-magnetic species such as Cr or B.

For SUL–SL, H_K^{eff} is found to be –6233 ± 88 Oe. Since $H_K \cong 12$ Oe $\ll 4\pi M_S$, $H_K^{eff} \cong -4\pi M_S$ can be used to estimate $M_S = 496 \pm 7$ emu cm^{-3}. This value is in excellent agreement with that measured by VSM (496 emu cm^{-3}). The fit of $\tau(H)$ leads to $\alpha = 0.0144 \pm 0.0005$ for SUL–SL.

FMR

FMR experiments are performed on MAG, SUL–SL, SUL+Tb–SL and SUL–SAF (table 1). In the case of sample MAG having a perpendicular anisotropy, the DC field is oriented perpendicular to film plane and the RF field is oriented parallel to the film plane. The easy-axis hysteresis loop measured perpendicular to the film plane is presented in figure 7(a). The measurable resonance field H_{FMR} is limited by the maximum frequency used in this study (40 GHz). In order to ensure a saturated magnetization state within the range of DC field corresponding to the FMR line, the DC field is stepped down from a value higher than the saturation

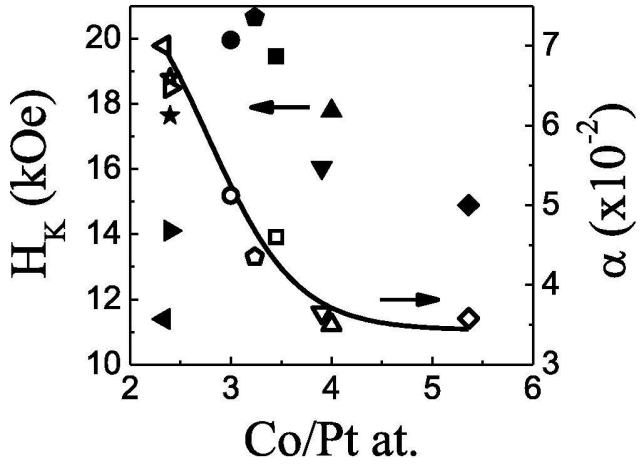

Figure 6. Anisotropy field H_K (solid symbols) and damping parameter α (empty symbols) as a function of Co/Pt atomic ratio for samples MAG1 (●), MAG2 (■), MAG3 (▲), MAG4 (▼), MAG5 (♦), CAP1 (►), CAP2 (◄), CAP2R (★) evaluated by TRMOKE; the values of H_K and α evaluated by FMR for sample MAG (⬟) are also presented.

field (typically 20 kOe) to −3 kOe. The RF frequency range $f = 35.5$–40 GHz is selected so that the FMR line can be captured in the DC field range extending from the nucleation field to positive saturation (figure 7(a)). The FMR curves $d\chi_{RF}/dH$ measured at several frequencies of the RF field (figure 7(b)) are fitted with an asymmetric Lorentzian using equation (B.1*p*) derived in appendix B. The fitting parameters are the resonance field H_{FMR}, the resonance linewidth $\Delta H = 2\Delta + \Delta H_0$ (equation (B.1*l*)), the mixing angle ε and a vertical scaling factor. The dependence of H_{FMR} on ω/γ_0, where $\omega = 2\pi f$ and $\gamma_0 = \mu_B/\hbar$, is presented in figure 7(c) and is used to extract H_K^{eff} and the Landé factor g_L based on equation (B.1*e*) which can be expressed as $H_{FMR} = -H_K^{eff} + \omega/(g_L\gamma_0)$ for the particular geometry used in this experiment. One obtains $g_L = 2.153 \pm 0.015$ and $H_K = 20\,647 \pm 88$ Oe using $M_S = 800$ emu cm^{-3} determined by VSM. Figure 7(d) presents the dependence of ΔH on ω/γ where $\gamma = g_L\gamma_0$. The latter is fitted using equation (B.1*k*) in order to extract the anomalous line broadening $\Delta H_0 = 443 \pm 133$ Oe and the damping parameter $\alpha = 0.044 \pm 0.005$. For sample MAG with Co/Pt of 3.24, the obtained value of α is consistent with the dependence of α on Co/Pt atomic ratio evaluated by TRMOKE (see sample MAG2 in table 1).

In the case of SUL–SL, the easy-axis direction is orientated in the film plane along the radial disk direction via the application of a DC magnetic field ~100 Oe during film deposition. The easy and the hard-axis hysteresis loops $M(H)$ measured by VSM under applied fields in the sample plane are presented in figure 8(a). The saturation magnetization evaluated by VSM is $M_S = 496$ emu cm^{-3}. FMR measurements on SUL–SL are performed at saturation, using in-plane DC and RF fields which are orthogonal to each other. At first, the DC field is orientated along the easy-axis. The FMR curves are measured for several RF frequencies in the range of 5–40 GHz with a 2.5 GHz step (figure 8(b)) and fitted using an asymmetric Lorentzian (appendix B) in order to extract H_{FMR}

HIGHLY CONFIDENTIAL - ATTORNEYS' EYES ONLY
MR Technologies GmbH
Ex. 2018, IPR2026-00016
Page 7 of 16
WD0293679
JX-2036.007

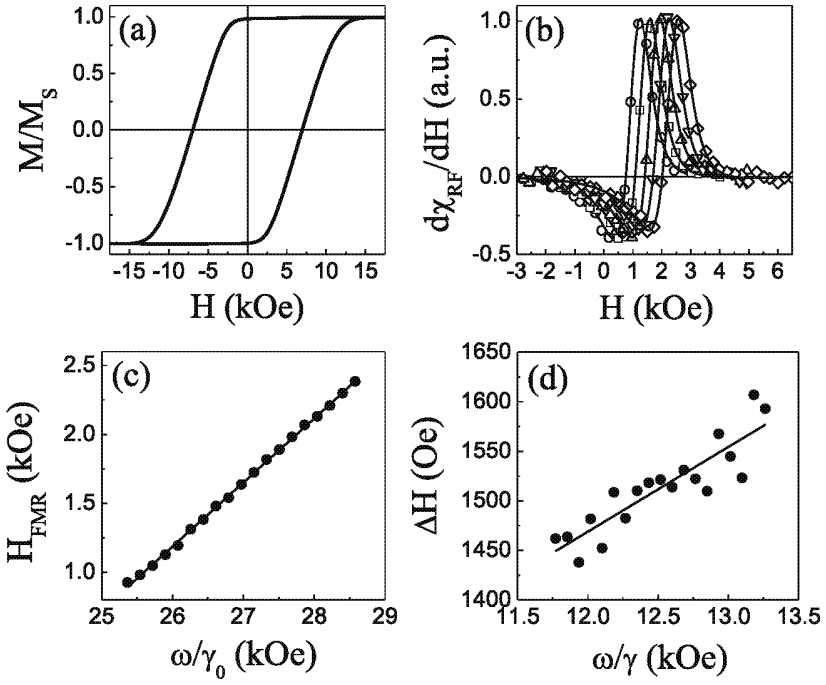

Figure 7. (a) Easy-axis hysteresis loop for sample MAG measured by polar-Kerr. (b) FMR absorption curves (symbols) measured for sample MAG using an applied field along the easy-axis (perpendicular to film plane) and asymmetric Lorentzian fit (solid line) for several RF frequencies f: 36 GHz (○), 37 GHz (□), 38 GHz (△), 39 GHz (▽) and 40 GHz (◇). (c) Resonance field H_{FMR} (symbols) as a function of ω/γ_0 (where $\omega = 2\pi f$, $\gamma_0 = \mu_B/\hbar$) and linear fit (solid line) used to extract $H_K^{eff} = H_K - 4\pi M_S$ (intercept) and Landé factor g_L (inverse of the slope). (d) FMR line width ΔH as a function of ω/γ (where $\gamma = g_L\gamma_0$) (solid symbols) and linear fit (solid line) used to extract the anomalous line broadening ΔH_0 (y-intercept) and the damping factor α (half of the slope).

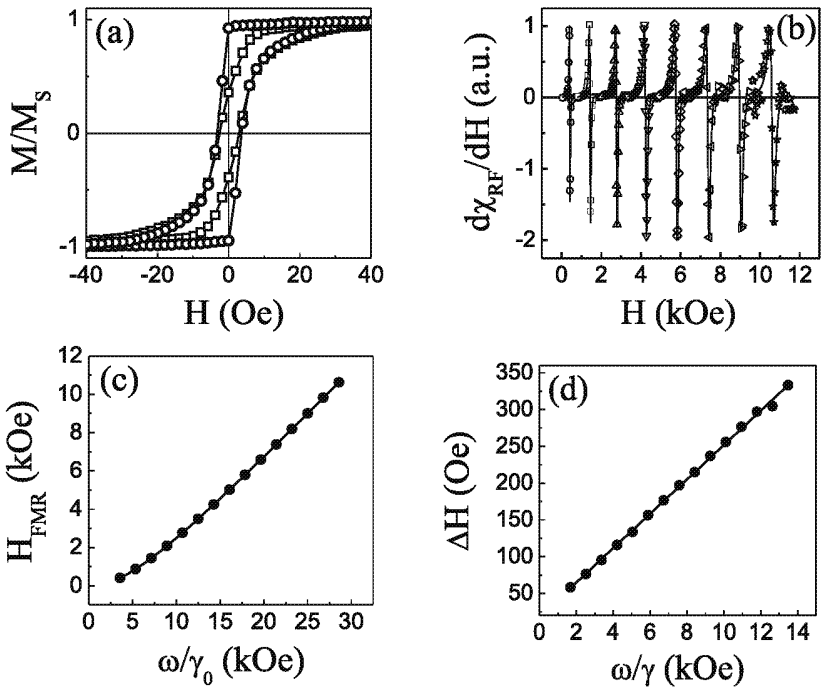

Figure 8. (a) In-plane easy (○) and hard-axis (□) hysteresis loops for SUL single-layer measured by VSM. (b) FMR absorption curves using an applied field along the easy-axis (in-plane) and asymmetric Lorentzian fit (solid line) for several RF field frequencies f: 5 GHz (○), 10 GHz (□), 15 GHz (△), 20 GHz (▽), 25 GHz (◇), 30 GHz (◁), 35 GHz (▷) and 40 GHz (☆). (c) Resonance field H_{FMR} as a function of ω/γ_0 (symbols) and fit (solid line) used to extract M_S and Landé factor g_L. (d) FMR linewidth ΔH as a function of ω/γ (solid symbols) and linear fit (solid line) used to extract ΔH_0 and α.

HIGHLY CONFIDENTIAL - ATTORNEYS' EYES ONLY
MR Technologies GmbH
Ex. 2018, IPR2026-00016 WD0293680
Page 8 of 16
JX-2036.008

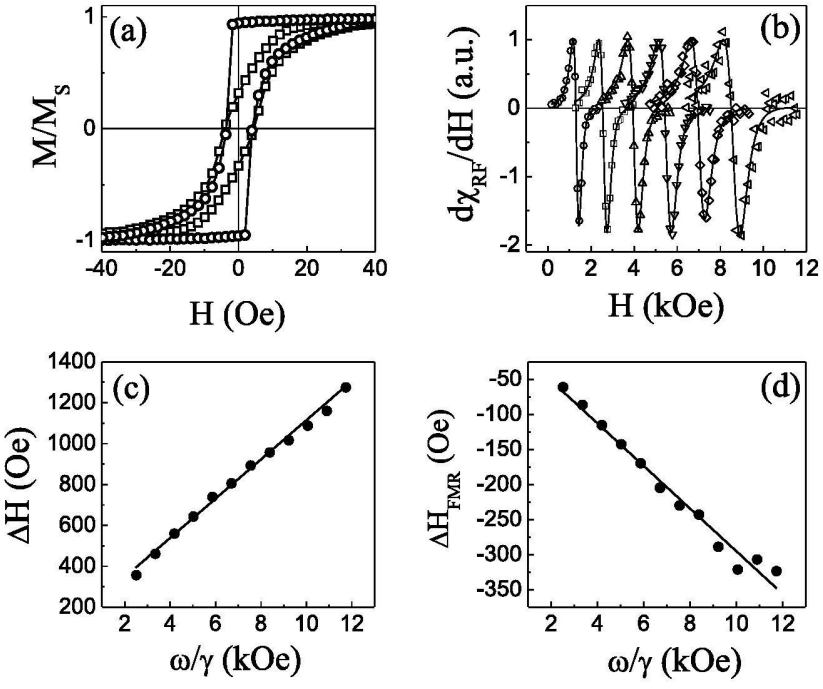

Figure 9. (a) In-plane easy (○) and hard-axis (□) hysteresis loops for single-layer SUL doped with 2% Tb measured by VSM. (b) FMR absorption curves using an applied field along the easy-axis (in-plane) and asymmetric Lorentzian fit (solid line) for several RF field frequencies f: 10 GHz (○), 15 GHz (□), 20 GHz (△), 25 GHz (▽), 30 GHz (◇) and 35 GHz (◁). (c) FMR linewidth ΔH as a function of ω/γ (●) and linear fit (solid line) used to extract ΔH_0 and α. (d) Dependence of $\Delta H_{FMR} = H_{FMR}^{SUL+Tb-SL} - H_{FMR}^{SUL-SL}$ on ω/γ.

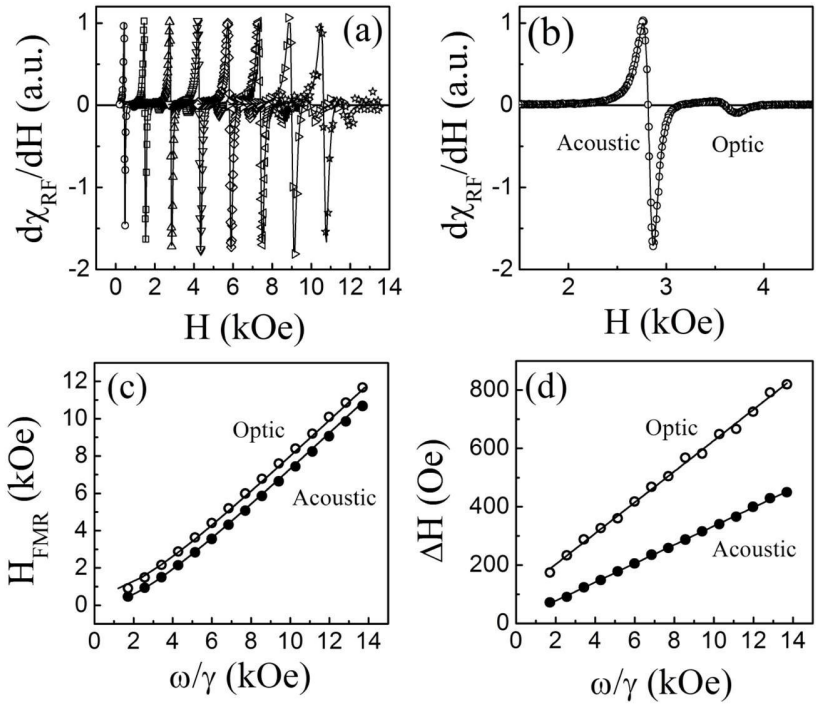

Figure 10. (a) FMR absorption curves (symbols) measured using an applied field along the easy-axis (in-plane) and asymmetric Lorentzian fit (solid line) for several RF field frequencies f: 5 GHz (○), 10 GHz (□), 15 GHz (△), 20 GHz (▽), 25 GHz (◇), 30 GHz (◁), 35 GHz (▷) and 40 GHz (☆). (b) Experimental FMR absorption curve for $f = 15$ GHz (symbols) and fit (solid line) showing the two resonance lines corresponding to the acoustic and optic precession modes of the two layer magnetizations. (c) Dependence of H_{FMR} corresponding to the acoustic (●) and optic (○) modes on ω/γ (symbols) and fit (solid line) using equation (B.3g) to evaluate J_{EX}. (d) FMR linewidths ΔH for the acoustic (●) and optic (○) modes as a function of ω/γ (solid symbols) and linear fit (solid line) used to evaluate ΔH_0 and α for both modes.

HIGHLY CONFIDENTIAL - ATTORNEYS' EYES ONLY
MR Technologies GmbH
Ex. 2018, IPR2026-00016 WD0293681
Page 9 of 16
JX-2036.009

and ΔH. The dependence of H_{FMR} on ω/γ_0 (figure 8(c)) is used to extract $M_S = 495 \pm 3$ emu cm^{-3} and the Landé factor $g_L = 2.13 \pm 0.003$ based on equation (B.2*f*) where H_K is assumed to be negligible. Figure 8(d) presents the dependence of ΔH on ω/γ and its linear fit is used to determine $\alpha = 0.012 \pm 0.0005$ and $\Delta H_0 = 18 \pm 1.8$ Oe based on equations (B.1*l*) and (B.2*d*). The obtained value of α is reasonably close to that evaluated by TRMOKE for SUL–SL (table 1).

In order to evaluate the anisotropy field H_K of the undoped SUL, FMR measurements are also performed at saturation using an in-plane DC field along the hard-axis and an in-plane RF field along the easy-axis of the SUL–SL sample. FMR curves are measured at various RF frequencies in the range of 5–40 GHz with a step of 5 GHz. The FMR curves were fitted using an asymmetric Lorentzian. The extracted values of H_{FMR} for DC field applied along the hard-axis are very close to those determined for DC field applied along the easy-axis. In this case, H_K can be estimated using equations (B.2*f*) and (B.2*g*) and the assumptions $H_K \ll 4\pi M_S$ and $H_K \ll H_{FMR}$. One obtains $H_K \cong \delta H_{FMR}\,(2H_{FMR} + 4\pi M_S)\,/\,(3H_{FMR} + 8\pi M_S)$, where δH_{FMR} is the difference between the H_{FMR} values for the hard and easy-axis direction of the DC field for the same frequency of the RF field. These values were averaged for all the RF frequencies, leading to $H_K = 11.9 \pm 2$ Oe.

The VSM hysteresis loops $M(H)$ for the sample SUL+Tb–SL measured using an in-plane applied field H along the easy and hard-axis directions are plotted in figure 9(a). As one can notice in figures 8(a) and 9(a), the easy and hard-axis loops for SUL+Tb–SL and SUL–SL have similar characteristics. For SUL+Tb–SL $H_C = 3.8$ Oe in the easy-axis and $H_C = 4.2$ Oe in the hard-axis directions, whereas for SUL–SL $H_C = 3.5$ Oe in the easy-axis and $H_C = 2.7$ Oe in the hard-axis directions. The results indicate that doping CoFeX with 2 at.% Tb does not significantly alter its soft magnetic properties.

FMR experiments are conducted on SUL+Tb–SL using an in-plane DC field along the easy-axis direction and an RF field in the frequency range of 5–40 GHz (figure 9(b)). The FMR curves are fitted using an asymmetric Lorentzian, and H_{FMR} and ΔH are extracted. Based on the observations of [17], g_L is not expected to be affected by Tb doping. Accordingly, the same value of g_L as for the undoped SUL–SL is used to fit the dependence of ΔH on ω/γ to extract $\Delta H_0 = 155 \pm 17$ Oe and $\alpha = 0.048 \pm 0.0011$ (figure 9(c)). The damping constant α of SUL+Tb–SL is four times larger than that of the undoped SUL–SL sample. The progressive increase of α in a Py film as a result of doping with 0–6 at.% Gd, Ho, Dy and Tb rare-earth (RE) atoms has been reported in [17] and interpreted based on the 'slow-relaxing' RE impurity model of [26]. According to the model, the RE 4*f* band is split as a result of the exchange interaction with its 5*d* band and the resulting 4*f* energy levels are thermally populated. The precession of the 3*d* electrons of the transition metal (TM = Co, Fe, Ni) modulates the RE Fermi energy. As a result, intraband transitions take place to repopulate the RE 4*f* energy levels. Due to the strong exchange coupling RE 5*d*–TM 3*d* and to the anisotropic exchange interaction RE 4*f*–5*d* (particularly important in the case of Tb atoms), the interaction RE 4*f*–5*d*—TM 3*d* leads to a magnetic field acting on the TM 3*d* orbital having a component perpendicular to its magnetic moment. This field has a stochastic character, being influenced by thermally activated RE 4*f* intraband transitions, leading to a complex Gilbert damping parameter α_{RE}. The real component of α_{RE} causes an increase of α and its imaginary component causes a negative shift of H_{FMR} proportional to the RF frequency in the case of RE-doped TM with respect to pure TM. This interpretation is supported by the measured dependence of $\Delta H_{FMR} = H_{FMR}^{SUL+Tb-SL} - H_{FMR}^{SUL-SL}$ on the RF frequency as shown in figure 9(d).

FMR measurements on the SUL–SAF sample are performed at saturation, using an in-plane DC field along the easy-axis and an in-plane RF field along the hard-axis. FMR curves measured at several RF field frequencies in the range of 5–40 GHz are shown in figure 10(a). As one can notice in figure 10(b), FMR spectra contain two resonance modes: the acoustic mode corresponds to an in-phase (symmetric) oscillation and the optic mode corresponds to 180° phase-shifted (antisymmetric) oscillation of the magnetizations of the two SUL layers [27]. As explained in appendix B, the fit of the resonance curve can be performed using a superposition of two asymmetric Lorentzians in order to extract H_{FMR} and ΔH for each of the two modes. The dependence of H_{FMR} on the RF frequency for the two modes are presented in figure 10(c). The acoustic mode has a higher resonance frequency or conversely a lower H_{FMR} than the optic mode. The curves are fitted using equation (B.3*g*) in order to evaluate the RKKY exchange coupling constant J_{EX} between the two magnetic layers of SUL–SAF. During the fit, M_S and g_L are set at the values determined for SUL–SL and J_{EX} is the only fitting parameter. One obtains $J_{EX} = 0.11 \pm 0.02$ erg cm^{-2}. The dependence of the resonance linewidth ΔH on the RF frequency for the two modes, presented in figure 10(d), are fitted using the equation $\Delta H = 2\alpha\frac{\omega}{\gamma} + \Delta H_0$ derived in appendix B in order to evaluate ΔH_0 and α for the two modes. One obtains $\alpha_{acoustic} = 0.016 \pm 0.0001$ and $\Delta H_{0,\,acoustic} = 12.9 \pm 1.7$ Oe for the acoustic mode, and $\alpha_{optic} = 0.0265 \pm 0.0004$ and $\Delta H_{0,\,optic} = 96.3 \pm 6.7$ Oe for the optic mode. The damping of the acoustic mode is expected to be degenerate with that of the SUL–SL, which is confirmed by the close values of α (table 1). The damping of the optic mode is higher than that of the acoustic mode. This has been evidenced previously on Py/Ru/Py structures [28] and explained based on the spin-pumping effect [29]. A moving magnetization vector in a ferromagnet (F) generates a spin current through a ferromagnet/normal-metal (F/N) interface. In an F/N/F trilayer, such as the SUL–SAF, both F layers are injecting a spin current into each other through the metallic (Ru) spacer which is thin enough to preserve the spin current polarization. The spin current pumped by the magnetic layer '*i*' into the magnetic layer '*j*' of an SUL–SAF dissipates by electron angular-momentum transfer leading to a torque acting on the magnetization of layer '*j*'. This effect leads to an additional damping term in the LLG equations describing the dynamics of the two F layer magnetizations [29]:

HIGHLY CONFIDENTIAL - ATTORNEYS' EYES ONLY
MR Technologies GmbH
Ex. 2018, IPR2026-00016
Page 10 of 16
WD0293682
JX-2036.010

$$\frac{d\hat{m}_i}{dt} = -\gamma\hat{m}_i \times \vec{H}_{eff,i} + \alpha\hat{m}_i \times \frac{d\hat{m}_i}{dt} + \alpha_{SP,i}\left(\hat{m}_i \times \frac{d\hat{m}_i}{dt} - \hat{m}_j \times \frac{d\hat{m}_j}{dt}\right) \quad (2)$$

where $\vec{H}_{eff,i}$ is the effective field acting on each layer magnetization (expressed in appendix B), $\alpha_{SP,\,i} = \gamma\hbar\tilde{g}^{FNF}_{\uparrow\downarrow}/(4\pi M_{S,i}t_i)$ is the spin-pumping damping parameter, t_i $(i = 1, 2)$ are the thicknesses, $M_{S,i}$ are the saturation magnetizations and α_i are the Gilbert damping parameters for the F layers. The factor $\tilde{g}^{FNF}_{\uparrow\downarrow}$ is the interfacial spin mixing conductance (*per* unit interface area) of the trilayer. If the two magnetic layers have the same thickness t and saturation magnetization M_S (which is the case of the investigated SUL–SAF), in the case of acoustic mode the spin-pumping term (last term in equation (2)) vanishes whereas for the optic mode it becomes $2\alpha_{SP,i}$ $(\hat{m}_i \times d\hat{m}_i/dt)$ leading to the following expressions for the total damping parameters:

$$\begin{cases} \alpha_{acoustic} = \alpha \\ \alpha_{optic} = \alpha + \gamma\hbar\tilde{g}^{FNF}_{\uparrow\downarrow}/(2\pi M_S t) \end{cases}. \quad (3)$$

By using equation (3) one obtains $\tilde{g}^{FNF}_{\uparrow\downarrow} = 11.25\,\mathrm{nm}^{-2}$. Since in the F/N/F trilayer, the spin current crosses two F/N interfaces, the conductance of the trilayer is that of two resistors in series. By assuming that the two F/N interfaces of the F/N/F trilayer are identical and since there are no other metallic layers in contact with the two F layers of the SUL–SAF that can act as spin sinks, the spin mixing conductance for a single F/N interface is $\tilde{g}^{FN}_{\uparrow\downarrow} = 2\tilde{g}^{FNF}_{\uparrow\downarrow} = 22.5\,\mathrm{nm}^{-2}$. This value is close to $\tilde{g}^{FN}_{\uparrow\downarrow} = 24\,\mathrm{nm}^{-2}$ reported for Py/Ru in [30].

It is evident from table 1 that both TRMOKE and FMR offer consistent values of damping constant α of the CoPtX–Y and CoFeX films with vastly different magnetic properties. The fact that TRMOKE can accurately evaluate Gilbert damping of both the recording layers and soft underlayer has important implications for further development of PMR media. TRMOKE offers several advantages over FMR for advanced characterization of magnetic films and multilayers: (a) TRMOKE is essentially a surface characterization technique that can be used to characterize only the top layer of a multilayered stack for its intrinsic properties (including damping and anisotropy field) that are important in controlling the switching behaviors of ECC media. In contrast, FMR has a much larger probing depth due to the frequency of the RF field being much lower than that of light, rendering the technique unsuitable for isolating the properties of top switching layer from the other layers. (b) TRMOKE is applicable to electrical conductive AlNiP substrates (commonly used in PMR media) as opposed to FMR which requires electrically insulating substrates.

Conclusions

The dependence of Gilbert damping constant α in CoPtX–Y granular alloys with perpendicular magnetic anisotropy on the Co/Pt atomic ratio is investigated using TRMOKE and FMR. It is shown that α increases monotonically from 0.03 to 0.07 with decreasing Co/Pt ratio from 5.5 to 2.5.This behavior is associated with the strong spin–orbit coupling of Pt 5*d* electrons which are polarized by the Co 3*d* electrons. By using reactive sputtering it is observed that oxidation of non-magnetic additives to CoPt, such as Cr and B, lead to their extraction from the composition of grain core. This has a much lower effect on the damping α than on H_K and M_S which are strongly enhanced (M_S is enhanced by 21% and H_K is enhanced by 25% by using 2% O_2 reactive sputtering). This is attributed to the lower sensitivity of α to the perturbation of the electronic band structure of grain core by non-magnetic species such as Cr and B.

For soft magnetic CoFeX films used as SUL in PMR media, TRMOKE and FMR offer consistent values of $\alpha \sim 0.012$. By doping the CoFeX film with 2 at.% Tb, α increases by a factor of four whereas the $M(H)$ hysteresis loop properties are not significantly affected. This effect is explained to be a consequence of the anisotropic exchange coupling of the Tb 4*f*–5*d* electronic bands causing the exchange field acting on the 3*d* electrons of the transition metals (Co, Fe) to become non-collinear with their moments. A balanced, synthetic antiferromagnet SUL having the structure CoFeX/Ru/CoFeX is also investigated by FMR. The resonance fields of the acoustic and optic oscillation modes are used to evaluate the interlayer exchange coupling constant $J_{EX} = 0.11$ erg cm^{-2} and their linewidths are used to determine the Gilbert damping parameters of the two modes. The higher damping of the optic mode with respect to the acoustic one is a consequence of spin pumping through the Ru space layer. The difference between the two damping constants is used to estimate the spin mixing conductance for the CoFeX/Ru interface $\tilde{g}^{FN}_{\uparrow\downarrow} = 22.5\,\mathrm{nm}^{-2}$.

Acknowledgments

Authors gratefully acknowledge the help received from R Admana and S Dang with VSM and polar-Kerr characterization.

Appendix A

TRMOKE: field dependence of frequency and damping time

Let us assume that the sample plane is parallel to the *xOy* plane of a Cartesian system of coordinates, the magnetocrystalline anisotropy axis being oriented along *Oz* (figure A1). The sample is submitted to the action of a DC field $\vec{H}$ oriented in the *yOz* plane under an angle θ_H with respect to the perpendicular to the film plane. The sample is assumed to be uniformly magnetized, of saturation magnetization $\vec{M}_S = M_S\hat{m}$ where $\hat{m} = (m_x, m_y, m_z)$ is the unit vector describing the orientation of $\vec{M}_S$. The effective field acting on the sample is $\vec{H}_{eff} = \left(0, H_y, H_z + H_K^{eff}m_z\right)$, where the effective anisotropy field is $H_K^{eff} = H_K - 4\pi M_S$, $H_K = 2K/M_S$ being the sample intrinsic anisotropy field. The free energy *per* unit film volume is:

HIGHLY CONFIDENTIAL - ATTORNEYS' EYES ONLY
MR Technologies GmbH
Ex. 2018, IPR2026-00016
Page 11 of 16
WD0293683
JX-2036.011

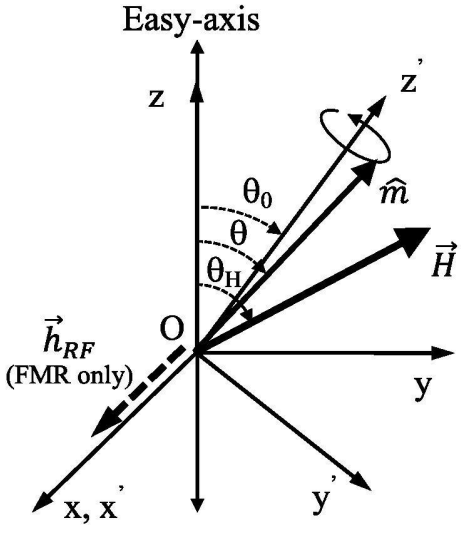

Figure A1. Schematics of a TRMOKE experiment illustrating the relative orientation of $\vec{H}$, $\vec{h}_{RF}$ and $\hat{m}$.

$$e = \frac{E}{V} = -K_{eff}\cos^2\theta - HM_S\cos\left(\theta - \theta_H\right) \qquad (A.1)$$

where $K_{eff} = H_K^{eff} M_S/2$ is the effective uniaxial anisotropy constant and θ is the polar angle describing the orientation of M_S. The equilibrium (minimum energy) orientation of M_S, $\theta = \theta_0$, can be found as the solution of the equation $de/d\theta = 0$:

$$\sin\left(2\theta_0\right) = \frac{2H}{H_K^{eff}}\sin\left(\theta_H - \theta_0\right). \qquad (A.2)$$

Let us select another cartesian coordinate system $x'y'z'$ which is obtained from xyz by rotating it around the Ox axis by the angle θ_0, such that the Oz' becomes parallel to the equlibrium orientation of M_S. In the new cordinate system $x'y'z'$, $\hat{m} = \left(m'_x, m'_y, m'_z\right)$, where $m'_x = m_x$, $m'_y = m_y\cos\theta_0 - m_z\sin\theta_0, m'_z = m_y\sin\theta_0 + m_z\cos\theta_0$, and the effective field $\vec{H}_{eff} = \left(0, m'_y H_1, H_2 - m'_y H_K^{eff}\sin\theta_0\cos\theta_0\right)$. Here, we have introduced the following notations:

$$\begin{cases} H_1 = H\cos\left(\theta_H - \theta_0\right) + H_K^{eff}\cos\left(2\theta_0\right) \\ H_2 = H\cos\left(\theta_H - \theta_0\right) + H_K^{eff}\cos^2\theta_0 \end{cases}. \qquad (A.3)$$

If the magnetization is slightly pulled out of the equilibrium direction, e.g. as a result of the heating effect of the pump pulse, the motion of the magnetization is described by the LLG equation:

$$\frac{d\hat{m}}{dt} = -\gamma\hat{m}\,x\,\vec{H}_{eff} + \alpha\hat{m}\,x\,\frac{d\hat{m}}{dt} \qquad (A.4)$$

where $\gamma = g_L\mu_B/\hbar$ is the gyromagnetic factor, g_L is the Landé factor, μ_B is the Bohr magneton and $\hbar = h/(2\pi)$ where h is the Plank constant. In the case of small deviation of M_S from the equilibrium direction, one can assume $m'_x \ll 1$, $m'_y \ll 1$ and $m'_z \cong 1$. In this case, equation (A.4) can be written as:

$$\begin{cases} \frac{dm'_x}{dt} = -\gamma m'_y H_1 - \alpha\frac{dm'_y}{dt} \\ \frac{dm'_y}{dt} = \gamma m'_x H_2 + \alpha\frac{dm'_x}{dt} \end{cases}. \qquad (A.5)$$

After performing a time derivative, the system of differential equation (A.5) can be decoupled:

$$\begin{cases} \frac{d^2m'_x}{dt^2}\left(1+\alpha^2\right) = -\alpha\gamma\left(H_1+H_2\right)\frac{dm'_x}{dt} - \gamma^2 H_1 H_2 m'_x \\ \frac{d^2m'_y}{dt^2}\left(1+\alpha^2\right) = -\alpha\gamma\left(H_1+H_2\right)\frac{dm'_y}{dt} - \gamma^2 H_1 H_2 m'_y \end{cases}. \qquad (A.6)$$

By assuming that $1+\alpha^2 \cong 1$, the solution of equation (A.6) is a damped harmonic oscillation having the expression:

$$\begin{cases} m'_x = m'_{x0}\exp\left(-i\omega t\right)\exp\left(-\frac{t}{\tau}\right) \\ m'_y = m'_{y0}\exp\left(-i\omega t\right)\exp\left(-\frac{t}{\tau}\right) \end{cases} \qquad (A.7)$$

where the angular frequency ω and the damping time τ are given by:

$$\omega = \gamma\sqrt{H_1 H_2} \qquad (A.8a)$$

$$\frac{1}{\tau} = \frac{1}{2}\alpha\gamma\left(H_1+H_2\right). \qquad (A.8b)$$

In the present TRMOKE experiment, the component of $\hat{m}$ along the Oz axis (i.e. m_z) is measured by the polar-Kerr effect. According to equation (A.7), $m_z = -m'_y\sin\theta_0 + m'_z\cos\theta_0 \approx -m'_y\sin\theta_0 + \cos\theta_0$ is oscillatory, having the angular frequency and time constants described by equations (A.8*a*) and (A.8*b*), respectively.

Appendix B

Ferromagnetic resonance (FMR): case of perpendicular anisotropy

In an FMR experiment, the sample is submitted to the action of two fields: a DC applied field H (similar to the TRMOKE experiment) orientated along the Oz axis and to an RF field h_{RF} orientated along the Ox axis in figure A1. By using the coordinate system $x'y'z'$ defined in appendix A ($m'_z \cong 1$), the LLG equation (A.4) can be expressed as:

$$\begin{cases} \frac{dm'_x}{dt} = -\gamma m'_y H_1 - \alpha\frac{dm'_y}{dt} \\ \frac{dm'_y}{dt} = -\gamma\left(h_{RF} - m'_x H_2\right) + \alpha\frac{dm'_x}{dt} \end{cases} \qquad (B.1a)$$

where H_1, H_2 are given by equation (A.3). Let us assume that the RF field has the expression $h_{RF} = h_{RF0}e^{-i\omega t}$ where $\omega = 2\pi f$, f being the RF frequency. In this case, the solutions of equation (B.1*a*) are:

$$\begin{cases} m'_x = m'_{x0}e^{-i\omega t} \\ m'_y = m'_{y0}e^{-i\omega t} \end{cases} \qquad (B.1b)$$

where m'_{x0} and m'_{y0} are complex amplitudes that can be found by replacing equation (B.1*b*) in equation (B.1*a*). The RF

HIGHLY CONFIDENTIAL - ATTORNEYS' EYES ONLY
MR Technologies GmbH
Ex. 2018, IPR2026-00016 WD0293684
Page 12 of 16
JX-2036.012

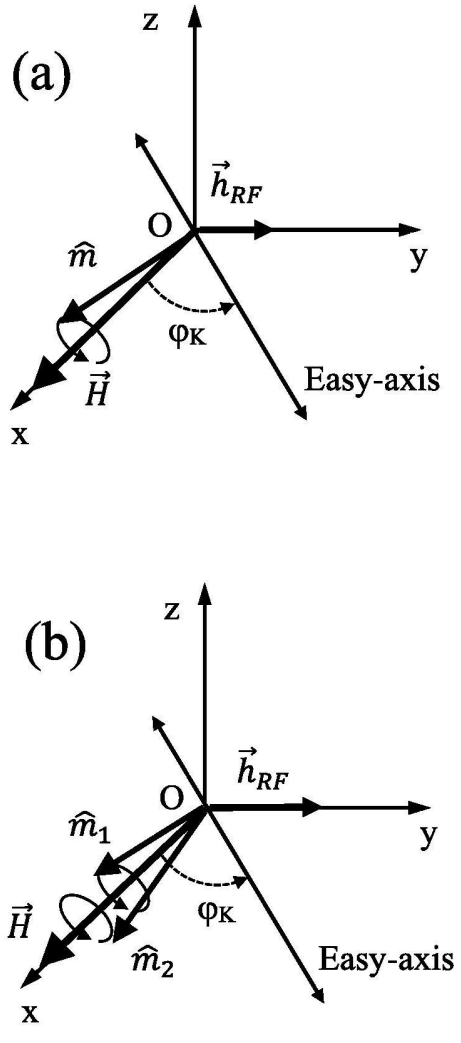

Figure B1. Schematics of an FMR experiment on: (a) single-layer SUL (SUL–SL); (b) synthetic antiferromagnetic SUL (SUL–SAF).

susceptibility measured along the direction Ox of the RF field, coinciding with Ox', is:

$$\chi_x = \chi_x' + i\chi_x'' = M_S \frac{m_x'}{h_{RF}} = M_S \frac{H_1 - i\alpha\frac{\omega}{\gamma}}{\left(H_1 - i\alpha\frac{\omega}{\gamma}\right)\left(H_2 - i\alpha\frac{\omega}{\gamma}\right) - \left(\frac{\omega}{\gamma}\right)^2} \tag{B.1c}$$

where H_1, H_2 are given by equation (A.3). The microwave power $P_{RF}(H)$ absorbed by a magnetic film *per* unit volume is given by:

$$P_{RF} = \frac{1}{2}\omega\chi_{RF}h_{RF0}^2 \tag{B.1d}$$

where $\chi_{RF} = \chi_x''$. The absorbed RF power P_{RF} is maximum at resonance. Therefore, in the absence of damping ($\alpha = 0$) the imaginary component $\chi_x'' \to \infty$. This is equivalent to vanishing denominator in equation (B.1*c*), leading to the following resonance condition:

$$\left(\frac{\omega}{\gamma}\right)^2 = H_1 H_2|_{H_{FMR}} \tag{B.1e}$$

where H_{FMR} is the resonance field. In order to extract the FMR linewidth ΔH, we introduce the following notations:

$$\begin{cases} H_1|_{H_{FMR}} = H_1^{FMR} \\ H_2|_{H_{FMR}} = H_2^{FMR} \end{cases}. \tag{B.1f}$$

Usually the resonance peak of $\chi_x''(H)$ is very sharp ($\Delta H \ll H_{FMR}$). Therefore, one can assume that in the range of applied fields corresponding to the resonance line:

$$H = H_{FMR} + \delta H \tag{B.1g}$$

where $\delta H \ll H_{FMR}$. Simple perturbation theory applied to equation (A.1) leads to the following expressions for the fields H_1 and H_2 defined in equation (A.3):

$$\begin{cases} H_1 = H_1^{FMR} + \Gamma\delta H \\ H_2 = H_2^{FMR} + \Pi\delta H \end{cases} \tag{B.1h}$$

where:

$$\begin{cases} \Gamma = \frac{H_{FMR} + H_K^{eff}[\cos(\theta_H - \theta_{FMR}) - \sin(2\theta_{FMR})\sin(\theta_H - \theta_{FMR})]}{H_1^{FMR}} \\ \Pi = \frac{H_{FMR} + H_K^{eff}\cos(\theta_H - \theta_{FMR})}{H_1^{FMR}} \end{cases}. \tag{B.1i}$$

By replacing equation (B.1*g*) in equation (B.1*c*), one obtains:

$$\begin{cases} \chi_x' = M_S \frac{H_1^{FMR}\left(\Pi H_1^{FMR} + \Gamma H_2^{FMR}\right)}{\left(H_1^{FMR} + H_2^{FMR}\right)^2} \frac{\delta H}{\Delta^2 + \delta H^2} \equiv C_1 \frac{\delta H}{\Delta^2 + \delta H^2} \\ \chi_x'' = M_S \frac{H_1^{FMR}}{\Pi H_1^{FMR} + \Gamma H_2^{FMR}} \frac{\Delta}{\Delta^2 + \delta H^2} \equiv C_2 \frac{\Delta}{\Delta^2 + \delta H^2} \end{cases} \tag{B.1j}$$

where:

$$\Delta = \frac{\Pi H_1^{FMR} + \Gamma H_2^{FMR}}{H_1^{FMR} + H_2^{FMR}} \alpha \frac{\omega}{\gamma}. \tag{B.1k}$$

It is worth noticing that the expression $F(H) = 1/\left(\Delta^2 + \delta H^2\right)$ appearing in equation (B.1*j*) is a Lorentz distribution having the center at $H = H_{FMR}$ (defining the FMR line position) and the full width at half maximum (usually called FMR linewidth) $\Delta H = 2\Delta$. In general, the FMR linewidth contains contributions unrelated to the intrinsic damping which are included in an additional term ΔH_0 (usually called anomalous line broadening) in the expression of the linewidth as:

$$\Delta H = 2\Delta + \Delta H_0. \tag{B.1l}$$

According to equation (B.1*e*), the dependence of the FMR line position $H = H_{FMR}$ on the frequency of the RF field enables the estimation of the effective anisotropy field H_K^{eff} and the Landé factor g_L. According to equation (B.1*k*), the dependence of the resonance linewidth ΔH on the RF frequency enables us to evaluate the damping parameter α. The line position and linewidth are usually extracted by fitting the FMR resonance curve to the derivative of an asymmetric Lorentzian. Asymmetry has to be considered because the coupling between the magnetic sample and microwave guide/cavity can mix real and imaginary parts of the RF susceptibility. Therefore, the measured RF susceptibility (equation (B.1*c*)) has the general expression:

HIGHLY CONFIDENTIAL - ATTORNEYS' EYES ONLY
MR Technologies GmbH
Ex. 2018, IPR2026-00016
Page 13 of 16
WD0293685
JX-2036.013

$$\chi_{RF} = \cos(\epsilon)\,\chi_x'' + \sin(\varepsilon)\,\chi_x' = \frac{C_2\Delta\cos(\epsilon) + C_1\delta H\sin(\epsilon)}{\Delta^2 + \delta H^2} \tag{B.1m}$$

where ε is the mixing angle between dispersive and absorptive components. If the detection of the RF susceptibility is performed using a lock-in technique by modulating the applied DC magnetic field H using an AC field (typically 100 Hz) which is applied along the same direction as the DC field and has an amplitude $h_{AC} \ll H$, the absorbed power P_{RF} (equation (B.1*d*)) becomes modulated with the AC component of the amplitude δP_{RF} given by:

$$\delta P_{RF} = \frac{1}{2}\omega h_{RF0}^2 \frac{d\chi_{RF}}{dH} h_{AC}. \tag{B.1n}$$

In this case, the measured signal is proportional to $d\chi_{RF}/dH$ rather then χ_{RF}. According to equation (B.1*m*), the measured signal is:

$$\frac{d\left[\cos(\epsilon)\,\chi_x'' + \sin(\varepsilon)\,\chi_x'\right]}{dH} = \frac{1}{\left(\Delta^2 + \delta H^2\right)^2} \left[C_1\sin(\epsilon)\left(\Delta^2 - \delta H^2\right) - 2C_2\cos(\epsilon)\,\Delta\delta H\right]. \tag{B.1o}$$

The fitting parameters of the FMR line are ϵ, H_{FMR} and Δ. In the particular case of the DC field H being perpendicular to the sample plane, $\theta_H = 0$, $\theta_0 = 0$, leading to $H_1^{FMR} = H_2^{FMR} = H_{FMR} + H_K^{eff}$, $\Gamma = \Pi = 1$, $C_1 = C_2 = M_S/2$, $\Delta = \alpha\omega/\gamma$, $H_{FMR} = \omega/\gamma - H_K^{eff}$. In this case equation (B.1*o*) becomes:

$$\frac{d\left[\cos(\epsilon)\,\chi_x'' + \sin(\varepsilon)\,\chi_x'\right]}{dH} = \frac{M_S}{2}\frac{\sin(\epsilon)\left(\Delta^2 - \delta H^2\right) - 2\cos(\epsilon)\,\Delta\delta H}{\left(\Delta^2 + \delta H^2\right)^2}. \tag{B.1p}$$

This equation is used in this work to fit the FMR line for a layer with perpendicular anisotropy.

FMR—case of single-layer SUL

Since the anisotropy field of a single-layer SUL is very low ($H_K \cong 12$ Oe), the FMR measurements are performed at saturation, using an external field $H > 100$ Oe applied in-plane either along the easy-axis or along the hard-axis of the SUL. Let us consider the geometry presented in figure B1(a), where the xOy plane of a Cartesian coordinate system is orientated parallel to the film plane. The applied field H is assumed to be orientated along the Ox axis, the RF field h_{RF} is oriented along the Oy axis and the magnetocrystalline anisotropy axis is orientated in the xOy plane at an angle φ_K with respect to Ox. Let us also assume that the sample is uniformly magnetized, having a saturation magnetization M_S. Since the FMR curve is measured in a range of DC fields $H \gg H_K$, the orientation of the effective anisotropy field H_{eff} acting on the film magnetization M_S (containing Zeeman, magnetostatic and magnetocrystalline contributions) is close to that of H. Consequently, M_S is orientated in the vicinity of the Ox axis ($m_x \cong 1$, $m_y \ll 1$, $m_z \ll 1$). The effective field H_{eff} acting on the film magnetization M_S is given by:

$$\overrightarrow{H}_{eff} = \begin{cases} H + H_K\cos^2\varphi_K + \frac{1}{2}H_K\sin(2\varphi_K)\,m_y \\ h_{RF} + H_K\sin^2\varphi_K m_y \\ -4\pi M_S m_z \end{cases}. \tag{B.2a}$$

By using the notations:

$$\begin{cases} H_1 = H + H_K\cos^2\varphi_K + 4\pi M_S \\ H_2 = H + H_K\cos(2\varphi_K) \end{cases} \tag{B.2b}$$

and following the same steps as in the preceding section (appendix B), we obtain the following expressions for the real and imaginary components of the RF susceptibility:

$$\begin{cases} \chi_y' = M_S\frac{H_1^{FMR}}{H_1^{FMR}+H_2^{FMR}}\frac{\delta H}{\Delta^2+\delta H^2} \equiv C\frac{\delta H}{\Delta^2+\delta H^2} \\ \chi_y'' = M_S\frac{H_1^{FMR}}{H_1^{FMR}+H_2^{FMR}}\frac{\Delta}{\Delta^2+\delta H^2} \equiv C\frac{\Delta}{\Delta^2+\delta H^2} \end{cases} \tag{B.2c}$$

where:

$$\Delta = \alpha\frac{\omega}{\gamma} \tag{B.2d}$$

and $\delta H = H - H_{FMR}$ where H_{FMR} is the solution of the resonance condition:

$$\left(\frac{\omega}{\gamma}\right)^2 = H_1 H_2\big|_{H_{FMR}}. \tag{B.2e}$$

In this case, $d\chi_{RF}/dH$ is expressed by equation (B.1*o*) where $C_1 \equiv C_2 = C$. The fitting parameters of the FMR line are ϵ, H_{FMR} and Δ. Two particular cases are studied in this paper:

(1) DC field is orientated along the easy-axis. In this case $\varphi_K = 0$, $H_1^{FMR} = H_2^{FMR} = H_{FMR} + H_K + 4\pi M_S$, $C = M_S/2$ leading to:

$$\frac{\omega}{\gamma} = \sqrt{\left(H_{FMR} + H_K + 4\pi M_S\right)\left(H_{FMR} + H_K\right)} \tag{B.2f}$$

(2) DC field is orientated along the hard-axis. In this case $\varphi_K = \pi/2$, $H_1^{FMR} = H_{FMR} + 4\pi M_S$ and $H_2^{FMR} = H_{FMR} - H_K$, $C = M_S\left(H_{FMR} + 4\pi M_S\right)/\left(2H_{FMR} - H_K + 4\pi M_S\right)$ leading to:

$$\frac{\omega}{\gamma} = \sqrt{\left(H_{FMR} + 4\pi M_S\right)\left(H_{FMR} - H_K\right)}. \tag{B.2g}$$

The FMR linewidth is given by equation (B.1*l*) where Δ is given by equation (B.2*d*).

FMR—case of SAF SUL

Let us consider the case of a synthetic-antiferromagnetic SUL, composed of two magnetic layers denominated in the following by '1' and '2' having the thicknesses t_i where $i = 1, 2$. Let us consider a Cartesian coordinate system having the xOy plane parallel to the surfaces of the two layers (figure B1(b)). The two layers are assumed to have uniaxial anisotropies, their easy-axes being orientated in the film plane at

HIGHLY CONFIDENTIAL - ATTORNEYS' EYES ONLY
MR Technologies GmbH
Ex. 2018, IPR2026-00016
Page 14 of 16
WD0293686
JX-2036.014

an angle φ_K with respect to the Ox axis. The anisotropy field H_K and saturation magnetization M_S of the two layers are assumed to be equal. The two layers are RKKY exchange coupled, the exchange coupling *per* unit film surface being J_{EX}. FMR measurements are performed close to saturation, using an applied field $H \gg H_{SAT}$ (~270 Oe) oriented along the Ox axis (easy-axis). In this case, the equilibrium orientations of the two layers magnetizations are close to the Ox axis, as shown in figure B1(b). Let us denote by $\hat{m}_i$ the unit vectors describing the orientation of the two layers magnetizations, $m_{i,x} \cong 1$, $m_{i,y} \ll 1$ and $m_{i,z} \ll 1$. The effective fields acting on each of the two layers are:

$$\vec{H}_{eff,i} = \begin{cases} H + H_K \cos^2\varphi_K + H_{EX,i} + \frac{1}{2} H_K \sin(2\varphi_K)\, m_{i,y} \\ h_{RF} + H_{EX,i} m_{j,y} + H_K \sin^2\varphi_K m_{i,y} \\ H_{EX,i} m_{j,z} - 4\pi M_S m_{i,z} \end{cases} \quad \text{(B.3}a\text{)}$$

where $j \neq i$ and $H_{EX,i} = -J_{EX}/(t_i M_S)$ are the exchange fields acting on the two magnetic layers. The LLG equation (A.4) for the two layers are:

$$\frac{d\hat{m}_i}{dt} = -\gamma \hat{m}_i x \vec{H}_{eff,i} + \alpha \hat{m}_i x \frac{d\hat{m}_i}{dt}. \quad \text{(B.3}b\text{)}$$

By assuming that $h_{RF} = h_{RF0} e^{-i\omega t}$ and:

$$\begin{cases} m_{i,y} = m_{i,y0} e^{-i\omega t} \\ m_{i,z} = m_{i,z0} e^{-i\omega t} \end{cases}. \quad \text{(B.3}c\text{)}$$

The normal oscillation modes, corresponding to $h_{RF} = 0$ and $\alpha = 0$, are the solution of $\det(\Lambda) = 0$:

$$\left[\left(\frac{\omega}{\gamma}\right)^4 - c_1 \left(\frac{\omega}{\gamma}\right)^2 + c_2\right]_{H=H_{FMR}} = 0 \quad \text{(B.3}g\text{)}$$

where:

$$\begin{cases} c_1 = A_1 B_1 + A_2 B_2 + 2 H_{EX,1} H_{EX,2} \\ c_2 = (A_1 A_2 - H_{EX,1} H_{EX,2})(B_1 B_2 - H_{EX,1} H_{EX,2}) \end{cases}. \quad \text{(B.3}h\text{)}$$

Among the four solutions of equation (B.3*g*) two are negative (unphysical) and two are positive. The lowest positive frequency corresponds to the so-called optic mode while the larger one corresponds to the acoustic mode. If the resonant line is narrow $H_{FMR} = H + \delta H$, one obtains the following expressions for the real χ_y' and imaginary χ_y'' components of the RF susceptibility $\chi_y = (M_S/h_{RF0})(m_{1,y} t_1 + m_{2,y} t_2)/(t_1 + t_2)$:

$$\begin{cases} \chi_y' = M_S \frac{d_1 t_1 + d_2 t_2}{d_3 (t_1 + t_2)} \frac{\delta H}{\Delta^2 + \delta H^2} \\ \chi_y'' = M_S \frac{d_1 t_1 + d_2 t_2}{d_3 (t_1 + t_2)} \frac{\Delta}{\Delta^2 + \delta H^2} \end{cases} \quad \text{(B.3}i\text{)}$$

where:

$$\Delta = \alpha \frac{\omega}{\gamma} \quad \text{(B.3}j\text{)}$$

and:

$$\begin{cases} d_1 = \left[\left(\frac{\omega}{\gamma}\right)^2 (H_{EX,1} - A_1) - (H_{EX,1})^2 H_{EX,2} + H_{EX,1} A_1 A_2 - H_{EX,1} H_{EX,2} B_2 + A_1 A_2 B_2\right]_{H=H_{FMR}} \\ d_2 = \left[\left(\frac{\omega}{\gamma}\right)^2 (H_{EX,2} - A_2) - (H_{EX,2})^2 H_{EX,1} + H_{EX,2} A_1 A_2 - H_{EX,2} H_{EX,1} B_1 + A_1 A_2 B_1\right]_{H=H_{FMR}} \\ d_3 = \left\{-\left[\left(\frac{\omega}{\gamma}\right)^2 + H_{EX,1} H_{EX,2}\right](A_1 + A_2 + B_1 + B_2) + B_1 B_2 (A_1 + A_2) + A_1 A_2 (B_1 + B_2)\right\}_{H=H_{FMR}} \end{cases}. \quad \text{(B.3}k\text{)}$$

Equation (B.3*b*) can be written as:

$$\Lambda \begin{pmatrix} m_{1,y} \\ m_{1,z} \\ m_{2,y} \\ m_{2,z} \end{pmatrix} = \begin{pmatrix} 0 \\ h_{RF0} \\ 0 \\ h_{RF0} \end{pmatrix} \quad \text{(B.3}d\text{)}$$

where:

$$\Lambda = \begin{pmatrix} -i\frac{\omega}{\gamma} & A_1 - i\alpha\frac{\omega}{\gamma} & 0 & -H_{EX,1} \\ B_1 - i\alpha\frac{\omega}{\gamma} & i\frac{\omega}{\gamma} & -H_{EX,1} & 0 \\ 0 & -H_{EX,2} & -i\frac{\omega}{\gamma} & A_2 - i\alpha\frac{\omega}{\gamma} \\ -H_{EX,2} & 0 & B_2 - i\alpha\frac{\omega}{\gamma} & i\frac{\omega}{\gamma} \end{pmatrix}. \quad \text{(B.3}e\text{)}$$

Here, we have used the following notations:

$$\begin{cases} A_i = H + H_K \cos^2\varphi_K + 4\pi M_S + H_{EX,i} \\ B_i = H + H_K \cos(2\varphi_K) + H_{EX,i} \end{cases}. \quad \text{(B.3}f\text{)}$$

In practice, in order to extract the resonant field H_{FMR} and the linewidth ΔH for the two resonant modes, the experimental dependence $\chi_{FMR}(H)$ is fitted in the least-squares sense by using a superposition of two independent Lorentzian resonant lines corresponding to the acoustic and optical modes. The linewidths of the acoustic and optic resonance modes are given by equation (B.1*l*) where Δ is given by equation (B.3*j*).

ORCID iDs

C Papusoi https://orcid.org/0000-0002-1973-8115

References

[1] Suess D, Schrefl T, Fähler S, Kirschner M, Hrkac G, Dorfbauer F and Fidler J 2005 *Appl. Phys. Lett.* **87** 012504
[2] Victora R H and Shen X 2005 *IEEE Trans. Magn.* **41** 537

HIGHLY CONFIDENTIAL - ATTORNEYS' EYES ONLY
MR Technologies GmbH
Ex. 2018, IPR2026-00016 WD0293687
Page 15 of 16
JX-2036.015

[3] Choe G and Ikeda Y 2014 *IEEE Trans. Magn.* **50** 5200704
[4] Thirion C, Wernsdorfer W and Mailly D 2003 *Nat. Mater.* **2** 524
[5] Boone C T, Katine J A, Marinero E E, Pisana S and Terris B D 2012 *J. Appl. Phys.* **111** 07B907
[6] Seki T, Utsumiya K, Nozaki Y, Imamura H and Takanashi K 2013 *Nat. Commun.* **4** 1726
[7] Kryder M H, Gage E C, McDaniel T W, Challener W A, Rottmayer R E, Ju G, Hsia Y T and Erden M F 2008 *Proc. IEEE* **96** 1810
[8] Weller D, Mosendz O, Parker G, Pisana S and Santos T S 2013 *Phys. Status Solidi* a **210** 1245
[9] Shimatsu T, Sato H, Oikawa T, Inaba Y, Kitakami O, Okamoto S, Aoi H, Muraoka H and Nakamura Y 2004 *IEEE Trans. Magn.* **40** 2483
[10] Shimatsu T, Sato H, Oikawa T, Inaba Y, Kitakami O, Okamoto S, Aoi H, Muraoka H and Nakamura Y 2005 *IEEE Trans. Magn.* **41** 566
[11] Inaba N, Uesaka Y, Nakamura A, Futamoto M, Sugita Y and Narishige S 1997 *IEEE Trans. Magn.* **33** 2989
[12] Mizukami S, Watanabe D, Kubota T, Zhang X, Naganuma H, Oogane M, Ando Y and Miyazaki T 2010 *Appl. Phys. Express* **3** 123001
[13] Mizukami S, Kubota T, Zhang X, Naganuma H, Oogane M, Ando Y and Miyazaki T 2011 *Japan. J. Appl. Phys.* **50** 103003
[14] Ju G, van de Veerdonk R J M, Tamaru S, Crawford T M, Parker G, Kubota Y, Lu M L, Batra S, Weller D and Bain J A 2002 *J. Appl. Phys.* **91** 8052
[15] Tahk Y W, Hong S Y, Hong D H, Lee H J and Lee T D 2004 *IEEE Trans. Magn.* **40** 2564
[16] Tahk Y W, Lee S C, Hong D H, Hong S Y and Lee T D 2004 *IEEE Trans. Magn.* **40** 2353
[17] Woltersdorf G, Kiessling M, Meyer G, Thiele J U and Back C H 2009 *Phys. Rev. Lett.* **102** 257602
[18] Montoya E, McKinnon T, Zamani A, Girt E and Heinrich B 2014 *J. Magn. Magn. Mater.* **356** 12
[19] Iihama S, Mizukami S, Inami N, Hiratsuka T, Kim G, Naganuma H, Oogane M, Miyazaki T and Ando Y 2013 *Japan. J. Appl. Phys.* **52** 073002
[20] Frolov S V and Vardeny Z V 1998 *Rev. Sci. Instrum.* **69** 1257
[21] van Kampen M, Jozsa C, Kohlhepp J T, LeClair P, Lagae L, de Jonge W J M and Koopmans B 2002 *Phys. Rev. Lett.* **88** 227201
[22] Malinowski G, Kuiper K C, Lavrijsen R, Swagten H J M and Koopmans B 2009 *Appl. Phys. Lett.* **94** 102501
[23] Kaufmann M D 2006 *PhD Thesis* University Gottingen
[24] Skomski R, Kashyap A and Sellmyer D J 2003 *IEEE Trans. Magn.* **39** 2917
[25] Kambersky V 1970 *Can. J. Phys.* **48** 2906
[26] van Vleck J H and Orbach R 1963 *Phys. Rev. Lett.* **11** 65
[27] Zhang Z, Zhou L and Wigen P E 1994 *Phys. Rev.* B **50** 6094
[28] Yang H, Li Y and Bailey W E 2016 *Appl. Phys. Lett.* **108** 242404
[29] Tserkovnyak Y, Brataas A, Bauer G E W and Halperin B I 2005 *Rev. Mod. Phys.* **77** 1375
[30] Behera N, Singh M S, Chaudhary S, Pandya D K and Muduli P K 2015 *J. Appl. Phys.* **117** 17A714

HIGHLY CONFIDENTIAL - ATTORNEYS' EYES ONLY
MR Technologies GmbH
Ex. 2018, IPR2026-00016
Page 16 of 16
WD0293688
JX-2036.016